Nanoscale

PAPER

View Article Online
View Journal | View Issue

Cite this: *Nanoscale*, 2018, **10**, 8578

Lead-free, air-stable hybrid organic–inorganic perovskite resistive switching memory with ultrafast switching and multilevel data storage†

Bohee Hwang[a] and Jang-Sik Lee *[a,b]

Received 30th January 2018,
Accepted 26th March 2018

DOI: 10.1039/c8nr00863a

rsc.li/nanoscale

Organolead halide perovskites exhibit excellent optoelectronic and photovoltaic properties such as a wide range of light absorption and tunable band gaps. However, the presence of toxic elements and chemical instability under an ambient atmosphere hindered lead halide perovskites from real device applications because of environmental issues and stability. Here, we demonstrate a resistive switching memory device based on a lead-free bismuth halide perovskite $(CH_3NH_3)_3Bi_2I_9$ (MABI). The active layer of the device can be easily prepared by solvent engineering. The nonvolatile memory based on MABI layers has reliable retention properties (~10^4 s), endurance (300 cycles), and switching speed (100 ns), as well as environmental stability. Moreover, the control of the compliance current leads to multilevel data storage with four resistance states, which can be applied to high-density memory devices. These results suggest that MABI has potential applications in information storage.

Introduction

Organic–inorganic lead (Pb) halide perovskites as solar cell absorbers have achieved high power conversion efficiencies (PCEs) up to 20%[1] due to a wide range of light absorption and long electron–hole diffusion lengths.[2–4] Despite the good device efficiency, the use of toxic lead (Pb) limits the large scale applications and commercialization. Therefore, lead-based perovskites need to be replaced by non-toxic alternatives. Methylammonium (CH_3NH_3; MA) bismuth halide perovskites with a chemical formula of $MA_3Bi_2I_9$ (MABI) are non-toxic, stable under humid conditions, and may have suitable semiconducting properties.[5–7] The Bi^{3+} cation, which has a lone pair of $6s^2$ electrons, improves stability due to the effect of screen-charged defects;[8,9] it also leads to interesting electro-optical properties[8,10,11] which can extend the application to optoelectronic and photovoltaic applications.[12–14] Moreover, because of these beneficial traits, bismuth halide perovskites have various applications such as in solar cell absorbers, supercapacitors, and memory applications.[13,15–17]

With the emerging demand for next-generation nonvolatile memory devices with a faster switching speed and better endurance, there are many types of memory architectures including phase-change random access memory (PRAM),[18] magnetic random access memory (MRAM),[19] and resistive switching random access memory (ReRAM)[20] to solve the demands. ReRAM devices, which are two terminal devices with electrode/active material/electrode capacitor-like structures, have been considered as promising candidates for nonvolatile information storage applications because of scalability, fast switching, and low power consumption.[20–22] Diverse materials systems show resistive switching behaviors; examples include organics,[23,24] transition metal oxides,[25,26] and perovskite oxides.[27,28]

Organic–inorganic hybrid perovskites (OIHPs) show hysteretic current–voltage (*I–V*) responses; they also have various advantages such as flexibility, multilevel data storage, analog switching, and possibility for low power consumption/high density memory applications.[29–36] Therefore, they have been used to fabricate resistive memory and synaptic devices.[37–39] OIHP materials are promising candidates for next-generation memory devices such as resistive switching memory devices for two reasons. First, OIHPs can have advantages of both inorganic and organic counterparts. As this material has an inorganic part, it has a possibility to show excellent resistive switching properties like oxides and chalcogenides. However, inorganic materials have a limitation to be applied in flexible electronics due to their brittleness. So, the organic parts such as A-site organic cations can extend their applications to flexible devices due to the structural flexibility of organic parts.[40] Second, OIHPs have a possibility to be applied in optical

[a]*Department of Materials Science and Engineering, Pohang University of Science and Technology (POSTECH), Pohang 37673, Korea. E-mail: jangsik@postech.ac.kr*
[b]*Department of Materials Science & Engineering, The University of Texas at Dallas, Richardson 75080, TX, USA*

†Electronic supplementary information (ESI) available. See DOI: 10.1039/c8nr00863a

memory. These days, in the field of optical communication, transferring optical signals with a high speed is an emerging issue for developing photon writing memory. As this material possesses light harvesting and light responsive properties, these properties lead to rapid progress in photo-sensing devices including photodiodes and phototransistors.[41] Recently, OIHP-based photo-memory with a heterojunction floating gate using a perovskite/PS blend has been demonstrated.[42] Moreover, utilizing the defect redistribution in OIHPs under light illumination extends their applications to photon-based neuromorphic computing.[43] For these reasons, it is meaningful to study the resistive switching effects using OIHP materials. Multilevel data storage can store more than two-data levels in a cell; the phenomenon can be exploited to increase the density of data storage effectively.[44] However, multilevel data storage has not been demonstrated in bismuth halide perovskites. Thus, to achieve the high-density memory device, a multilevel memory device based on MABI could lead to high-density perovskite ReRAM that does not have the issues of containing lead and a lack of stability under ambient conditions.

In this study, we demonstrated lead-free perovskite ReRAM based on MABI as a switching layer in nonvolatile memory devices. The MABI layer was synthesized on the indium tin oxide (ITO)-coated glass substrate by using an anti-solvent assisted solution process to obtain a uniform layer. The memory device based on MABI exhibits reliable bipolar resistive switching with reasonable retention and endurance, and also stability under an ambient atmosphere for at least 5 months. Moreover, by tuning the magnitude of the compliance current (CC), the device can elicit four distinct resistance states in the devices. This study demonstrates that MABI has potential applications in high-density memory.

Results and discussion

We fabricated MABI-based ReRAMs with the device structure Au/MABI/ITO (Fig. 1a). MABI exhibits a hexagonal symmetry; it is composed of layers of face-sharing BiI_6 bioctahedra; the voids between the layers are occupied by MA^+ groups.[45,46] A uniform perovskite layer is formed in the memory device; the MABI film is 250 nm thick (Fig. 1b). The crystal structure of MABI was determined using X-ray diffraction (Fig. 1c). The diffraction peaks matched well with the hexagonal system with the space group $P6_3/mmc$ as described in previous reports,[17,47] with the doublet peak near $2\theta = \sim 12°$. The optical absorption spectra of MABI films had a band edge near 500 nm, and the calculated band gap value is 2.19 eV which is consistent with previous reports.[5] (Fig. 1d).

The electrical properties of Au/MABI/ITO were determined under ambient conditions. The measured *I–V* curves exhibit bipolar resistive switching under a compliance current CC = 1 mA. To measure the *I–V* characteristics of the Au/MABI/ITO device, the voltage was controlled by one of the Au electrodes under a dc sweeping voltage applied as 0 V → 2 V → 0 V → −2 V → 0 V; the bottom electrode (ITO) was grounded. During

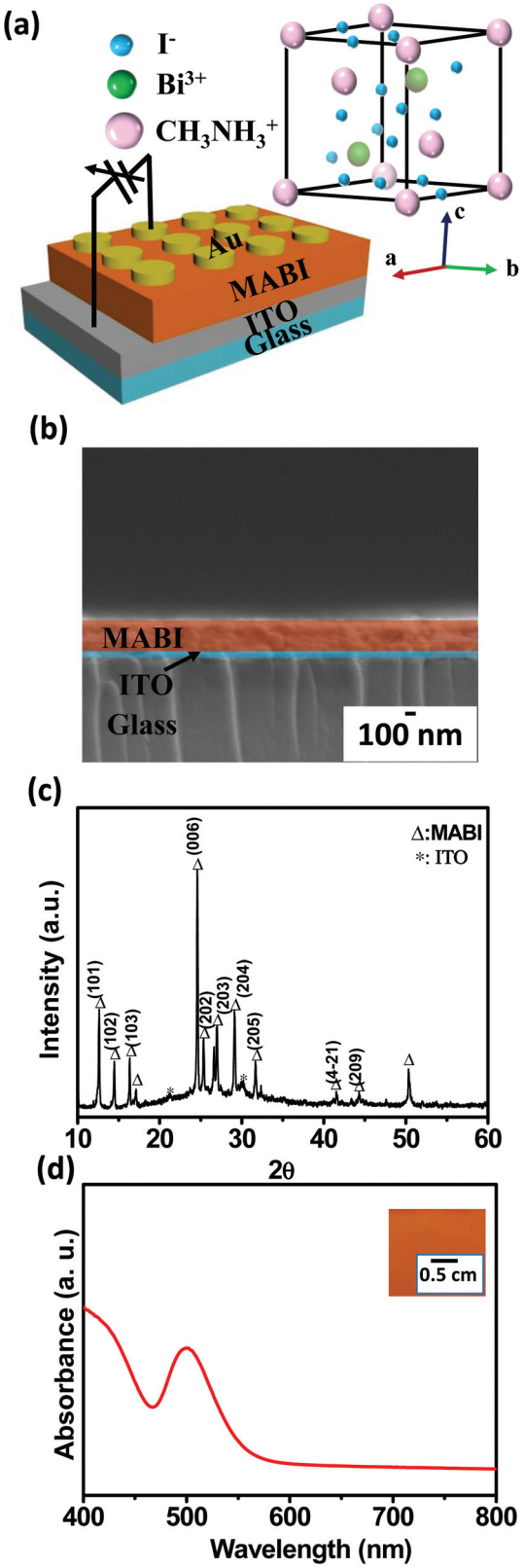

Fig. 1 (a) Schematic illustration of the memory device with the Au/MABI/ITO structure. The inset shows the MABI structure in a unit cell. (b) Cross-sectional SEM image of the MABI film. (c) XRD pattern of the MABI layer. (d) Absorption spectrum of the MABI thin film.

the first voltage sweep from 0 to 2 V, the 'set' process occurred at 1.6 V; during this process, the resistance changed from the high-resistance state (HRS, OFF state) to the low-resistance state (LRS, ON state). When a negative voltage was applied, the current decreased gradually at the reset voltage $V_{set} < -0.6$ V; the resistance changed from the LRS to the HRS (Fig. 2a). Data retention was evaluated to confirm the stability of the memory device with a read voltage of 0.2 V under ambient conditions (Fig. 2b). The LRS current slightly fluctuated, but overall the ON and OFF states were well distinguished up to 10^4 s. The cycling endurances of the Au/MABI/ITO devices were measured using consecutive ac voltage pulses to appraise the electrical stability under V_{set} = 3 V and V_{reset} = −3 V (Fig. 2c). The width of the voltage pulse was 10 ms and the read voltage was 0.2 V.

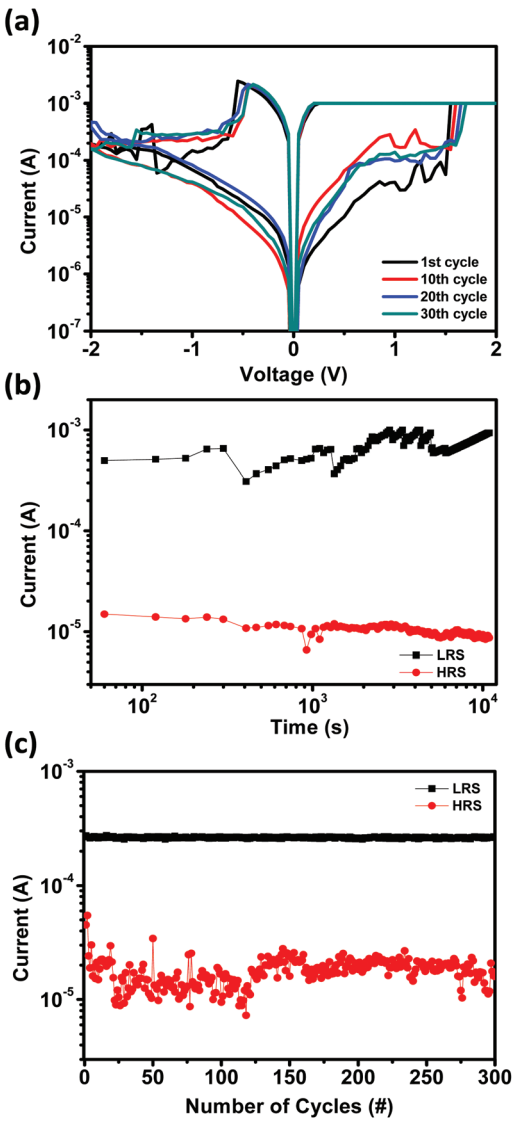

Fig. 2 (a) *I*–*V* characteristics of the Au/MABI/ITO device. (b) Data retention of the LRS and the HRS at room temperature. (c) Switching endurance of the memory device based on MABI.

The endurance properties varied over time, but neither the LRS nor the HRS degraded for 300 cycles. The statistical distribution of the HRS and LRS levels of the MABI device is shown (Fig. S1†). 10 individual devices showed a very small range of resistance level distribution in the HRS and LRS. The HRS and LRS differed by approximately two orders of magnitude (on/off ratio ~100). This indicates that MABI-based memory devices are electrically uniform and reliable.

The switching speed is an important attribute of memory devices; it can be obtained from the pulse width of V_{set} and V_{reset}. The MABI-based memory device responded quickly when V_{set} and V_{reset} were applied (Fig. 3a and b). Before and after applying the voltage pulses, a dc voltage bias sweep (0 to 0.7 V) was applied to check the device state. 'Set' and 'reset' processes do not occur in this voltage range, so the voltage bias sweep did not cause resistive switching. After bias pulses were applied using a pulse generator, a dc bias voltage sweep was applied to confirm the resistance change of the device. A set voltage pulse (3 V, 100 ns) and a reset voltage pulse (−3 V, 100 ns) were used to switch the devices' resistance state; the 100 ns pulse width was sufficient to switch resistance states. This switching speed is faster than the program speed of flash

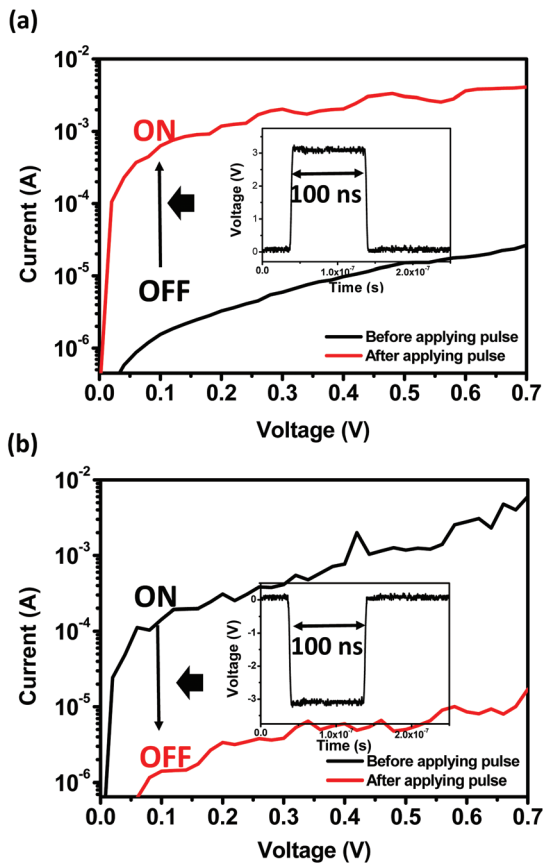

Fig. 3 *I*–*V* curves of the OFF and the ON states of the Au/MABI/ITO device before and after the application of (a) a set voltage pulse (3 V, 100 ns) and (b) a reset voltage pulse (−3 V, 100 ns). (Insets: Applied bias pulses.)

memory devices (order of microseconds),[48] so MABI-based memory is suitable for use in commercial memory devices. We also used consecutive ac voltage pulses to evaluate the electrical reliability with 100 ns pulse width. We applied 100 pulses (pulse width: 100 ns) to the device and read at 0.2 V to confirm the device state (Fig. S2†). The endurance properties were able to be determined at 100 ns pulse width for 400 cycles. The fast switching of bismuth perovskites might originate from the inherent properties of MABI. In the case of MABI, interactions between Bi 6s and I 5p orbitals induce partial antibonding orbital character at its valence band maximum. This antibonding orbital contribution to the valence band maximum and disperse conduction band leads to the improvement of tolerance to an intrinsic defect which induces shallow point defect states.[8,9] Bi^{3+} possesses a high Born effective charge,[8] and this potentially leads to better carrier transport properties.[49] The defect states which might function as trap states have a possibility to be filled quickly by charge carriers, and this achieves a faster switching speed than lead-based perovskites. In the organic bistable device, an electric field induced charge transfer was dominant which led to the fast switching speed.[50] A further study will be held to investigate the reason for the faster switching speed of bismuth-perovskites. Multilevel resistive switching behavior, which is very attractive since this enables us to store more than two data levels in one cell and also increases memory capacities, could be realized in the MABI-based memory device. We obtained three distinct LRS levels by using CC = 1 mA, 500 μA, or 100 μA (Fig. 4a). The resistance of the HRS was almost unaffected by different compliance currents, but the resistance of the LRS increased as the compliance current decreased. This result proves that the LRS can be tuned by using different compliance currents during the set process; this phenomenon can lead to multilevel states of the LRS. To confirm the reliability of multilevel switching, we measured the number of cycles for which the MABI-based ReRAM device was stable. The resistance states were determined at read voltage V_{read} = 0.2 V and CC = 1 mA, 500 μA, or 100 μA. Multilevel-switching was achieved with three LRSs and a stable HRS. The data levels exhibited distinct resistances for 10 cycles in each multilevel resistance state (Fig. 4b). We also measured the multibit information storage capability by using ac endurance (Fig. S3†). The width of the voltage pulse was 10 ms and the read voltage was 0.2 V.

The different resistance states could be distinguished for compliance currents of 1 mA, 500 μA, and 100 μA. To have practical applications in electronic devices, materials and devices need to be stable. Most of the methylammonium lead halide perovskites are not stable under humid conditions and an ambient atmosphere, and need to be fabricated under an N_2 atmosphere.[51] In previous studies, methylammonium lead halide perovskite (or cesium lead halide perovskite) based memory was reported using metal oxide layers as the protective layer for long-term stability.[52,53] However, in MABI, the outer lone pair of $6s^2$ electrons improves its stability under ambient conditions.[8] To evaluate the long-term stability, we stored the

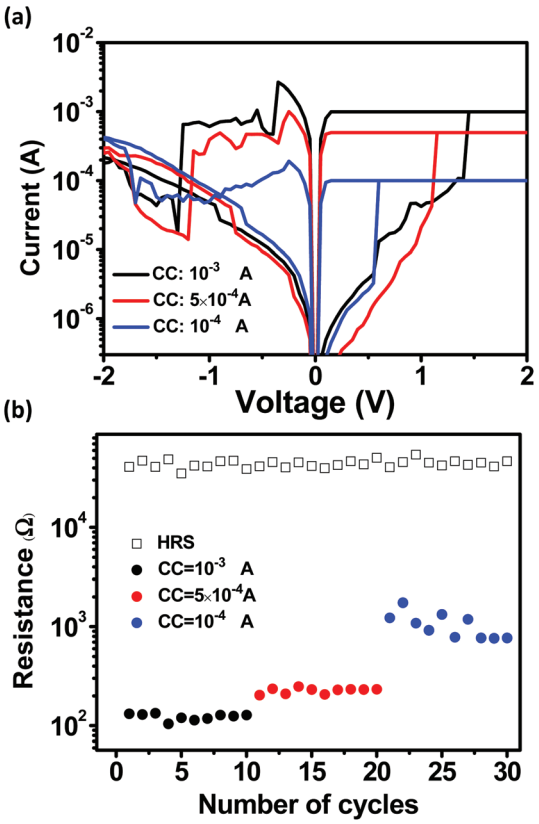

Fig. 4 (a) Typical *I*–*V* characteristics of the memory device under different compliance currents of 1 mA, 500 μA, and 100 μA. (b) Multilevel resistance states with different compliance currents.

MABI-based memory device under an ambient atmosphere at 23–25 °C and with 50–60% humidity. The XRD patterns of the MABI thin film were almost the same when measured on the 1st day of the synthesis and after 30 days of storage under ambient conditions (Fig. 5a). Additionally, there is almost no change in film quality (inset in Fig. 5a); this result suggests that the MABI thin film is stable without encapsulation layers. We also compared the surface roughness of the pristine MABI film and the film that was stored in ambient air for 5 months by atomic force microscopy (AFM) (scan size = 3 μm × 3 μm) (Fig. S4†) The pristine MABI film had a root mean square (RMS) roughness of 12.2 nm, and the film stored in air for 5 months showed a RMS roughness of 12.6 nm. This proves that the microstructure of the film almost did not change during storage in air for 5 months. The resistive switching properties of the MABI film did not degrade after the storage in air for 30 days (Fig. 5b). We further characterized the electrical properties to confirm the long-term stability. The electrical properties of the MABI devices (the devices were fabricated 5 months ago) were determined (Fig. S5†). The MABI devices were even operated 5 months after fabrication and showed bipolar resistive switching under a CC = 1 mA. Since 9 different devices operate well at the micrometer scale, the device is supposed to operate well at a smaller scale. These

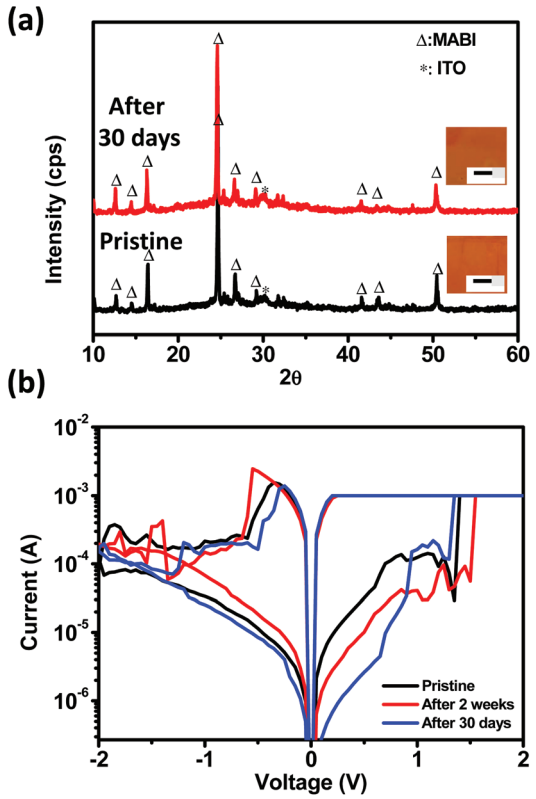

Fig. 5 (a) XRD patterns of the MABI film over time with air exposure. (Inset: Photographs of the pristine MABI film and the film stored in air for 30 days. The scale bar is 0.5 cm.) (b) Electrical properties of the Au/MABI/ITO device after storage in ambient air.

results indicate that MABI has potential to be used in practical applications. The conduction mechanism was interpreted for Au/MABI/ITO devices by considering $\log I$–$\log V$ plots during positive and negative voltage sweeps (Fig. S6†). The curve indicates that the conduction mechanisms of the LRS and HRS in the MABI layer can be explained by ohmic conduction and space-charge-limited conduction (SCLC). In the LRS region, ohmic conduction was dominant; this observation is consistent with the formation of conductive filaments in the MABI films. In the HRS region, the *I*–*V* characteristics show two different regions: at a low voltage (<0.4 V), the curves follow Ohm's law ($I \propto V$), whereas at a high voltage (>0.4 V), they show a relationship that corresponds to the trap-filled limit current law ($I \propto V^2$) (Fig. S6b†). At a 0–0.4 V low voltage region in the HRS, the electric field across the device is insufficient, so the quantity of injected carriers is less than that of thermally generated free charge carriers; therefore, trapsites are only partially filled, so the *I*–*V* curve obeys ohmic behavior. At a higher voltage (>0.4 V) during the voltage transition from ohmic to SCLC, all trap sites become occupied by charge carriers because of the increased electric field, and the conduction mechanism follows ($I \propto V^2$). When a negative bias (0 → −2 V) was applied, ohmic behavior is also observed. Applying the bias from −2 to 0 V changed the conduction from SCLC to ohmic (Fig. S6c†). The multilevel property in the MABI film could be explained by the conduction mechanism. Until now, the origin of the multilevel memory properties has remained controversial. In the previous studies, the compliance current[54] or the maximum voltage[55] was controlled to engineer the size of the conductive filaments which induce the multilevel property. In our current work, the origin of the multilevel property could be related to charge trapping and detrapping processes under different electric fields utilizing the compliance current. As a rapid conversion from ohmic to SCLC, this indicates the existence of traps in the MABI film (Fig. S6†). The traps are dispersed at different energy levels in the perovskite film.[56] The filling rate of the traps would be different with different compliance currents. For example, at the low compliance current, trap sites will be partially filled, so this induces a higher resistance state than the high compliance current. Also, we fabricated MABI-based memory devices using different metal electrodes to confirm the effect of electrode materials. Ag and Al were used as the top electrodes, and similar resistive switching behaviors were obtained when the Au electrode was used (Fig. S7†). The SCLC mechanism that was demonstrated in the *I*–*V* curves suggests that charge-trapping sites may be formed in the MABI layer. OIHPs can include various point defects such as Schottky defects (vacancies), Frenkel defects (interstitials), cation substitutions, and antisite substitutions.[57] The charged defects can migrate when subjected to an electric field. Among the point defects, iodide vacancies have the lowest activation barrier (~0.58 eV)[58] for ionic migration, and they are highly mobile. Thus, we suggest that resistive switching behavior may result both from charge trapping and detrapping under the electric field, and from iodide vacancy-mediated migration,[59] or the accumulation of I^- at the anode/perovskite interfaces[38,43] (Fig. S8†). The crystal structure of MABI can be explained by perovskite-like fragments which stack along the *c*-axis. The $Bi_2I_9^{3-}$ group alternates with $CH_3NH_3^+$ cations[45] (Fig. S8a†). In the case of iodide vacancy mediated migration, when a positive bias is applied, positively-charged iodide vacancies move toward the negatively charged ITO electrode during the set process. As the charge carriers are injected from the electrode, iodide vacancies combine with injected charge carriers and become neutralized. Moreover, the MABI structure has a face-sharing BiI_6 octahedral structure, so iodide vacancies can move easily along the edges of the octahedron. As the applied bias increases, iodide vacancies and the combination of charge carriers form conductive filaments that connect the bottom electrode to the top electrode (Fig. S8b†). When a negative bias is applied, electrons are detrapped during the 'reset' process, and the filaments rupture (Fig. S8c†). Also, the accumulation of I^- at the anode/MABI interface could be the reason for resistive switching as in the previous studies.[38] When the resistive switching process changes from the HRS to the LRS, I^- ions can be moved to the anode and potentially stored inside the electrode materials. This leads to the creation of iodide vacancies in the perovskite film, and a high concentration of iodide vacancies is formed near the cathode. As the voltage increases, iodide vacancy

regions will expand toward the anode, and this extended iodide vacancy region may form a conductive bridge between the electrodes. However, when the applied bias is removed, I atoms which are stored near the anode may diffuse as I^- ions (Au anode: $I^- \leftrightarrow I + e^-$) and diffused I^- will combine with the iodide vacancies in the perovskite film, resulting in the rupture of the filament[38,43]

Conclusions

In summary, we fabricated lead-free resistive switching memory devices based on MABI. The uniform film was formed using the anti-solvent assisted solution method. The fabricated device showed reproducible and reliable bipolar resistive switching behavior with a reasonable data retention time ($\sim 10^4$ s) and endurance (300 cycles). The application of different compliance currents to MABI memory devices elicited the multilevel switching property to at least four data levels. This study demonstrates that MABI has the potential to be used in high-density memory applications. This work provides an approach to achieve the applications of bismuth-based perovskites in information storage.

Methods

Perovskite deposition and device fabrication

MABI precursors were formed by dissolving CH_3NH_3I (0.75 mol) and BiI_3 (0.33 mol) in 1 ml of a dimethylformamide (DMF) (0.7 ml)/dimethyl sulfoxide (DMSO) (0.3 ml) solvent mixture. The perovskite layer was formed using anti-solvent assisted crystallization.[45] Before device fabrication, the ITO/glass substrate was cleaned with isopropyl alcohol and then with deionized water, and was then treated using UV/O_3 (wavelengths = 253.7 nm and 184.9 nm). The solution was coated at 500 rpm for 10 s, then the rotation was accelerated to 4000 rpm and held for 10 s; then, chlorobenzene was added dropwise onto the center of the substrate during spin-coating. The film was annealed at 70 °C for 10 min to remove residual elements. Finally, dot-shaped Au electrodes were deposited on the perovskite layer by evaporation through a shadow mask.

Perovskite characterization

The morphological images of the surface and cross-section were captured using a high-resolution FE-SEM (JEOL) with a 10 kV acceleration voltage and AFM (VEECO). The crystal structure was determined using XRD (Rigaku D/MAX-2500) with Cu Kα radiation at a step size of 0.02°. Current–voltage characteristics were determined using a Keithley 4200 in a vacuum probe station under an ambient atmosphere.

Conflicts of interest

There are no conflicts to declare.

Acknowledgements

This work was supported by the National Research Foundation of Korea (NRF-2016M3D1A1-27663). This work was also supported by the Future Semiconductor Device Technology Development Program (10045226) funded by the Ministry of Trade, Industry & Energy (MOTIE)/Korea Semiconductor Research Consortium (KSRC). In addition, this work was partially supported by the Brain Korea 21 PLUS project (Center for Creative Industrial Materials).

Notes and references

1 D. Q. Bi, C. Y. Yi, J. S. Luo, J. D. Decoppet, F. Zhang, S. M. Zakeeruddin, X. Li, A. Hagfeldt and M. Gratzel, *Nat. Energy*, 2016, **1**, 16142.
2 S. D. Stranks, G. E. Eperon, G. Grancini, C. Menelaou, M. J. P. Alcocer, T. Leijtens, L. M. Herz, A. Petrozza and H. J. Snaith, *Science*, 2013, **342**, 341–344.
3 Q. F. Dong, Y. J. Fang, Y. C. Shao, P. Mulligan, J. Qiu, L. Cao and J. S. Huang, *Science*, 2015, **347**, 967–970.
4 D. J. Yu, F. Cao, Y. L. Shen, X. H. Liu, Y. Zhu and H. B. Zeng, *J. Phys. Chem. Lett.*, 2017, **8**, 2565–2572.
5 B. W. Park, B. Philippe, X. L. Zhang, H. Rensmo, G. Boschloo and E. M. J. Johansson, *Adv. Mater.*, 2015, **27**, 6806–6813.
6 Y. C. Qiu, W. Liu, W. Chen, W. Chen, G. M. Zhou, P. C. Hsu, R. F. Zhang, Z. Liang, S. S. Fan, Y. G. Zhang and Y. Cui, *Sci. Adv.*, 2016, **2**, e1501764.
7 M. Q. Lyu, J. H. Yun, M. L. Cai, Y. L. Jiao, P. V. Bernhardt, M. Zhang, Q. Wang, A. J. Du, H. X. Wang, G. Liu and L. Z. Wang, *Nano Res.*, 2016, **9**, 692–702.
8 R. L. Z. Hoye, R. E. Brandt, A. Osherov, V. Stevanovic, S. D. Stranks, M. W. B. Wilson, H. Kim, A. J. Akey, J. D. Perkins, R. C. Kurchin, J. R. Poindexter, E. N. Wang, M. G. Bawendi, V. Bulovic and T. Buonassisi, *Chem. – Eur. J.*, 2016, **22**, 2605–2610.
9 R. E. Brandt, V. Stevanovic, D. S. Ginley and T. Buonassisi, *MRS Commun.*, 2015, **5**, 265–275.
10 T. Kawai and S. Shimanuki, *Phys. Status Solidi B*, 1993, **177**, K43.
11 T. Kawai, A. Ishii, T. Kitamura, S. Shimanuki, M. Iwata and Y. Ishibashi, *J. Phys. Soc. Jpn.*, 1996, **65**, 1464–1468.
12 M. Y. Leng, Z. W. Chen, Y. Yang, Z. Li, K. Zeng, K. H. Li, G. D. Niu, Y. S. He, Q. C. Zhou and J. Tang, *Angew. Chem., Int. Ed.*, 2016, **55**, 15012–15016.
13 T. Singh, A. Kulkarni, M. Ikegami and T. Miyasaka, *ACS Appl. Mater. Interfaces*, 2016, **8**, 14542–14547.
14 M. Q. Kong, H. Hu, L. Wan, M. M. Chen, Y. S. Gan, J. Wang, F. X. Chen, B. H. Dong, D. Eder and S. M. Wang, *RSC Adv.*, 2017, **7**, 35549–35557.
15 Z. Zhang, X. Li, X. Xia, Z. Wang, Z. Huang, B. Lei and Y. Gao, *J. Phys. Chem. Lett.*, 2017, **8**, 4300–4307.

16 Y. Q. Hu, S. F. Zhang, X. L. Miao, L. S. Su, F. Bai, T. Qiu, J. Z. Liu and G. L. Yuan, *Adv. Mater. Interfaces*, 2017, **4**, 1700131.
17 J. K. Pious, M. L. Lekshmi, C. Muthu, R. B. Rakhi and V. C. Nair, *ACS Omega*, 2017, **2**, 5798–5802.
18 K.-F. Kao, C.-M. Lee, M.-J. Chen, M.-J. Tsai and T.-S. Chin, *Adv. Mater.*, 2009, **21**, 1695–1699.
19 C. Chappert, A. Fert and F. N. Van Dau, *Nat. Mater.*, 2007, **6**, 813–823.
20 T. C. Chang, K. C. Chang, T. M. Tsai, T. J. Chu and S. M. Sze, *Mater. Today*, 2016, **19**, 254–264.
21 F. Pan, S. Gao, C. Chen, C. Song and F. Zeng, *Mater. Sci. Eng., R*, 2014, **83**, 1–59.
22 J. J. S. Yang, D. B. Strukov and D. R. Stewart, *Nat. Nanotechnol.*, 2013, **8**, 13–24.
23 X. F. Cheng, X. Hou, W. H. Qian, J. H. He, Q. F. Xu, H. Li, N. J. Li, D. Y. Chen and J. M. Lu, *ACS Appl. Mater. Interfaces*, 2017, **9**, 27847–27852.
24 S. J. Liu, P. Wang, Q. Zhao, H. Y. Yang, J. Wong, H. B. Sun, X. C. Dong, W. P. Lin and W. Huang, *Adv. Mater.*, 2012, **24**, 2901–2905.
25 C. Q. Hu, M. D. McDaniel, A. Posadas, A. A. Demkov, J. G. Ekerdt and E. T. Yu, *Nano Lett.*, 2014, **14**, 4360–4367.
26 A. R. Lee, G. H. Baek, T. Y. Kim, W. B. Ko, S. M. Yang, J. Kim, H. S. Im and J. P. Hong, *Sci. Rep.*, 2016, **6**, 30333.
27 H. Nili, S. Walia, S. Balendhran, D. B. Strukov, M. Bhaskaran and S. Sriram, *Adv. Funct. Mater.*, 2014, **24**, 6741–6750.
28 R. Yasuhara, T. Yamamoto, I. Ohkubo, H. Kumigashira and M. Oshima, *Appl. Phys. Lett.*, 2010, **97**, 132111.
29 C. Gu and J. S. Lee, *ACS Nano*, 2016, **10**, 5413–5418.
30 J. Choi, S. Park, J. Lee, K. Hong, D. H. Kim, C. W. Moon, G. D. Park, J. Suh, J. Hwang, S. Y. Kim, H. S. Jung, N. G. Park, S. Han, K. T. Nam and H. W. Jang, *Adv. Mater.*, 2016, **28**, 6562–6567.
31 W. Xu, H. Cho, Y. H. Kim, Y. T. Kim, C. Wolf, C. G. Park and T. W. Lee, *Adv. Mater.*, 2016, **28**, 5916–5922.
32 B. H. Hwang, C. W. Gu, D. H. Lee and J. S. Lee, *Sci. Rep.*, 2017, **7**, 43794.
33 B. Hwang and J. S. Lee, *Adv. Mater.*, 2017, **29**, 170104.
34 J.-Y. Seo, J. Choi, H.-S. Kim, J. Kim, J.-M. Yang, C. Cuhadar, J. S. Han, S.-J. Kim, D. Lee, H. W. Jang and N.-G. Park, *Nanoscale*, 2017, **9**, 15278–15285.
35 J. Choi, Q. V. Le, K. Hong, C. W. Moon, J. S. Han, K. C. Kwon, P. R. Cha, Y. Kwon, S. Y. Kim and H. W. Jang, *ACS Appl. Mater. Interfaces*, 2017, **9**, 30764–30771.
36 J. S. Han, Q. V. Le, J. Choi, K. Hong, C. W. Moon, T. L. Kim, H. Kim, S. Y. Kim and H. W. Jang, *Adv. Funct. Mater.*, 2018, **28**, 1705783.
37 E. Ercan, J.-Y. Chen, P.-C. Tsai, J.-Y. Lam, S. C.-W. Huang, C.-C. Chueh and W.-C. Chen, *Adv. Electron. Mater.*, 2017, **3**, 1700344.
38 X. J. Zhu, J. Lee and W. D. Lu, *Adv. Mater.*, 2017, **29**, 1700527.
39 Z. G. Xiao and J. S. Huang, *Adv. Electron. Mater.*, 2016, **2**, 1600100.
40 C. C. Stoumpos, C. D. Malliakas and M. G. Kanatzidis, *Inorg. Chem.*, 2013, **52**, 9019–9038.
41 W. Tian, H. P. Zhou and L. Li, *Small*, 2017, **13**, 1702107.
42 J. Y. Chen, Y. C. Chiu, Y. T. Li, C. C. Chueh and W. C. Chen, *Adv. Mater.*, 2017, **29**, 1702217.
43 X. Zhu and W. D. Lu, *ACS Nano*, 2018, **12**, 1242–1249.
44 H. Wang, F. B. Meng, Y. R. Cai, L. Y. Zheng, Y. G. Li, Y. J. Liu, Y. Y. Jiang, X. T. Wang and X. D. Chen, *Adv. Mater.*, 2013, **25**, 5498–5503.
45 M. Abulikemu, S. Ould-Chikh, X. H. Miao, E. Alarousu, B. Murali, G. O. N. Ndjawa, J. Barbe, A. El Labban, A. Amassiana and S. Del Gobbo, *J. Mater. Chem. A*, 2016, **4**, 12504–12515.
46 C. S. Ni, G. Hedley, J. Payne, V. Svrcek, C. McDonald, L. K. Jagadamma, P. Edwards, R. Martin, G. Jain, D. Carolan, D. Mariotti, P. Maguire, I. Samuel and J. Irvine, *Nat. Commun.*, 2017, **8**, 170.
47 K. Eckhardt, V. Bon, J. Getzschmann, J. Grothe, F. M. Wisser and S. Kaskel, *Chem. Commun.*, 2016, **52**, 3058.
48 S. K. Vishwanath and J. Kim, *J. Mater. Chem. C*, 2016, **4**, 10967–10972.
49 A. J. Lehner, D. H. Fabini, H. A. Evans, C. A. Hebert, S. R. Smock, J. Hu, H. B. Wang, J. W. Zwanziger, M. L. Chabinyc and R. Seshadri, *Chem. Mater.*, 2015, **27**, 7137–7148.
50 R. J. Tseng, J. X. Huang, J. Ouyang, R. B. Kaner and Y. Yang, *Nano Lett.*, 2005, **5**, 1077–1080.
51 M. Gratzel, *Nat. Mater.*, 2014, **13**, 838–842.
52 B. Hwang and J. S. Lee, *Sci. Rep.*, 2017, **7**, 673.
53 Y. Wu, Y. Wei, Y. Huang, F. Cao, D. J. Yu, X. M. Li and H. B. Zeng, *Nano Res.*, 2017, **10**, 1584–1594.
54 Y. Wang, Q. Liu, S. B. Long, W. Wang, Q. Wang, M. H. Zhang, S. Zhang, Y. T. Li, Q. Y. Zuo, J. H. Yang and M. Liu, *Nanotechnology*, 2010, **21**, 045202.
55 V. Kannan, V. Senthilkumar and J. K. Rhee, *J. Phys. D: Appl. Phys.*, 2013, **46**, 095301.
56 J. Kim, S. H. Lee, J. H. Lee and K. H. Hong, *J. Phys. Chem. Lett.*, 2014, **5**, 1312–1317.
57 J. M. Azpiroz, E. Mosconi, J. Bisquert and F. De Angelis, *Energy Environ. Sci.*, 2015, **8**, 2118–2127.
58 C. Eames, J. M. Frost, P. R. F. Barnes, B. C. O'Regan, A. Walsh and M. S. Islam, *Nat. Commun.*, 2015, **6**, 7497.
59 D. J. Kim, Y. J. Tak, W. G. Kim, J. K. Kim, J. H. Kim and H. J. Kim, *Adv. Mater. Interfaces*, 2017, **4**, 1601035.